Chalmers Publication Library

Chalmers Publication Library

Copyright Notice

(Article begins on next page)

Phase-to-phase and phase-to-amplitude transfer characteristics of a nondegenerate-idler phase-sensitive amplifier

Carl Lundström,* Zhi Tong, Magnus Karlsson, and Peter A. Andrekson

Photonics Laboratory, Department of Microtechnology and Nanoscience,
Chalmers University of Technology, S-412 96, Göteborg, Sweden
*Corresponding author: carl.lundstrom@chalmers.se

For the first time to our knowledge, the phase-to-phase and phase-to-amplitude transfer functions of a nondegenerate-idler phase-sensitive fiber optic parametric amplifier are experimentally measured. Additionally, analytically and numerically obtained transfer curves show excellent agreement with the experimental curves. The experimental results were obtained by imposing a linear phase modulation onto the signal and idler wave simultaneously, and detecting the input and output signal using a self-homodyne coherent receiver.   © 2011 Optical Society of America
OCIS codes: 060.2320, 190.4380.

Phase-sensitive amplifiers (PSAs) have recently attracted significant experimental attention [1–3] because of their unique properties, namely, a 0 dB quantum-limited noise figure [4,5] and the possibility to perform phase regeneration of phase-encoded data [6]. Phase-sensitive (PS) fiber optical amplifiers are based on four-wave mixing (FWM) [7], which is inherently a phase-sensitive process. However, if one of the interacting waves (the idler) is not initially present, it will be generated from noise in the process, giving a relative phase relation among the waves that is stable and independent of the input phases. In other words, the FWM process in such a case is phase insensitive (PI) with regard to the input signal phase. In the more general case, where all of the interacting waves are present at the input, the FWM process becomes dependent on the input phases of the waves. Aside from the full frequency nondegenerate case involving four distinct waves, there are two kinds of frequency non-degenerate FWM configurations that provide PS FWM. In the degenerate-idler configuration, a signal is symmetrically surrounded in the frequency domain by two pumps, while in the nondegenerate-idler (degenerate pump) configuration, a single pump is symmetrically surrounded by a signal and an idler that carry correlated phase information.

While FWM has been well studied both theoretically and experimentally, a detailed investigation of the response to input signal phase of a PS parametric amplifier has yet to be demonstrated. Preliminary experimental results were shown in [8], and in this Letter, we present analytical and experimental phase-to-phase and phase-to-amplitude transfer curves of a nondegenerate-idler PSA, for the first time, to the best of our knowledge.

With the undepleted pump approximation, the input–output relation of a nondegenerate PSA is [7]

$$\begin{bmatrix} A_s \\ A_i^* \end{bmatrix} = \begin{bmatrix} \mu & \nu \\ \nu^* & \mu^* \end{bmatrix} \begin{bmatrix} A_{s,0} \\ A_{i,0}^* \end{bmatrix}, \tag{1}$$

where A is the complex amplitude, subscripts s and i denote signal and idler waves, subscript 0 denotes the input condition, superscript $*$ represents the conjugation

operation, and μ and ν are the complex transfer coefficients, which satisfy the auxiliary equation $|\mu|^2 - |\nu|^2 = 1$. This is called a two-mode squeezing transformation [7]. Rewriting in terms of power and phases, denoting the signal and idler powers P_s and P_i, and their phases ϕ_s and ϕ_i, the output signal power becomes

$$P_s = |\mu|^2 P_{s0} + |\nu|^2 P_{i0} + 2|\mu||\nu|\sqrt{P_{s0}P_{i0}} \cdot \cos(\Delta_\phi), \quad (2)$$

with $\Delta_\phi = \phi_\mu - \phi_\nu + \phi_{s0} + \phi_{i0}$. The output signal phase can then be written as

$$\phi_s$$
$$= \arctan\left[\frac{|\mu|\sqrt{P_{s0}}\sin(\phi_\mu + \phi_{s0}) + |\nu|\sqrt{P_{i0}}\sin(\phi_\nu + \phi_{i0})}{|\mu|\sqrt{P_{s0}}\cos(\phi_\mu + \phi_{s0}) + |\nu|\sqrt{P_{i0}}\cos(\phi_\nu + \phi_{i0})}\right], \tag{3}$$

with similar expressions for the idler. In the above equations, ϕ_μ and ϕ_ν denote the argument of the complex transfer coefficients. Clearly, the signal output power and phase depend on the input power and phase of both signal and idler. It is instructive to consider the ideal case of perfect phase matching, where the FWM is maximally efficient. Then, $\mu = \cosh(g_0 L)$ and $\nu = i \sinh(g_0 L)$, where $g_0 = \gamma P_p$, with γ, P_p, and L denoting the nonlinearity coefficient, pump power, and length of the fiber PSA, respectively. The output signal power then becomes

$$P_s = P_{s0} + (P_{s0} + P_{i0})\sinh^2(g_0 L)$$
$$+ \sinh(2g_0 L)\sqrt{P_{s0}P_{i0}}\sin(\phi_{s0} + \phi_{i0}), \tag{4}$$

which, in the case of equal signal and idler input power and phase, can be simplified further to

$$P_s = P_{s0}[\cosh(2g_0 L) + \sinh(2g_0 L) \cdot \sin(2\phi_{s0})], \tag{5}$$

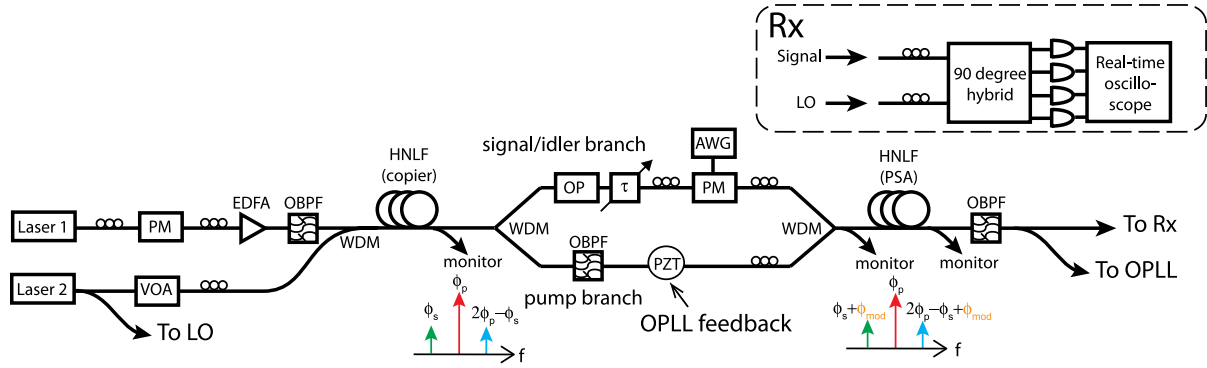which has extremes of $P_{s0} \cdot \exp(\pm 2g_0 L)$. The signal phase becomes

Fig. 1.   (Color online) Experimental setup. The acronyms are explained in the text.

$$\phi_s = \arctan\left[\frac{\cosh(2g_0L)\sin(\phi_{s0}) + \sinh(2g_0L)\cos(\phi_{s0})}{\cosh(2g_0L)\cos(\phi_{s0}) + \sinh(2g_0L)\sin(\phi_{s0})}\right],$$

(6)

where identical signal and idler input power and phase have also been assumed. In the limit $g_0L \gg 1$, Eq. (6) reduces to arctan(1), independently of signal phase, meaning that the output phase is squeezed into two discrete states. (Note that, while arctan(1) equals $\pi/4$ and $5\pi/4$, we have in the results below defined the two squeezed states as having phase 0 and π, for convenience.)

In addition to the dependence on signal and idler phase, from Eqs. (2) and (3) it is clear that both the output signal power and phase are dependent on the ratio between input signal and idler power, as well as on the complex transfer coefficients. We demonstrate several examples of these effects below.

The experimental setup is shown in Fig. 1. The copier generated three phase-correlated waves through FWM. Two fiber lasers at 1554.1 and 1545.0 nm (fixed wavelengths) were used as the pump source and signal, respectively. The pump was phase modulated with three RF tones to suppress stimulated Brillouin scattering (SBS) prior to amplification by a high-power erbium-doped fiber amplifier (EDFA) and filtering by two optical bandpass filters (OBPFs). Power from the signal laser was tapped off to be used as the local oscillator (LO) in the receiver, while the remaining power was attenuated with a variable optical attenuator (VOA). The pump and signal were combined by a wavelength division multiplexing (WDM) coupler and passed into the copier where an idler wave was generated. The copier was implemented in highly nonlinear fiber (HNLF) with length, zero dispersion wavelength (λ_0), and nonlinearity coefficient (γ) of 150 m, 1553.6 nm, and 10(W · km)$^{-1}$, respectively. After the copier, the pump and signal/idler were separated into separate branches by another WDM coupler. The powers of the signal and idler were controlled by a programmable optical processor (OP). The signal and idler were then phase modulated by a phase modulator (PM), driven by an electrical signal from an arbitrary waveform generator (AWG). A piezoelectric transducer (PZT)-based optical phase-locked loop (OPLL) compensated for slow phase drifts between the two arms. The pump was then recombined with the signal and idler by another WDM coupler, and injected into the PSA, which was implemented with a 250 m HNLF

with length, λ_0, and γ of 250 m, 1542 nm, and 11.7(W · km)$^{-1}$. This HNLF provided close to maximum gain at the signal wavelength when pumped at 1554.1 nm. Polarization controllers were used to align the waves at each stage. The PSA output signal was filtered and split, with one part being used for the OPLL feedback signal and the other part combined with the LO by a 90° optical hybrid. The hybrid outputs, corresponding to the two quadratures of the signal, were detected using balanced detection with a real-time sampling oscilloscope. For the OPLL feedback, the signal was detected with a low-noise 125 MHz photodiode and fed into a lock-in amplifier, giving a feedback signal proportional to the amplitude of a weak dither frequency component in the kilohertz range. The feedback signal was amplified by an inverting amplifier and a high-voltage amplifier before driving the PZT. The OPLL was stable for much longer than the measurement times.

The insets in Fig. 1 show the frequency allocation and phases of the interacting waves after the copier and prior to the PSA. At the PSA input, the signal and idler have a linear phase modulation over all phase states, allowing the full PSA phase response to be measured. The period of this modulation was tens of nanoseconds. In Fig. 2(a), phase and amplitude transfer curves of a nondegenerate-idler PSA are calculated from Eqs. (2) and (3), while Fig. 2(b) shows the experimentally measured curves. The experimental data agree very well with the analytical theory. In calculating the complex transfer coefficients μ and ν, the parameters of the PSA HNLF were used, with the pump power being the only fitting parameter. Moreover, the experimental data was low-pass filtered in
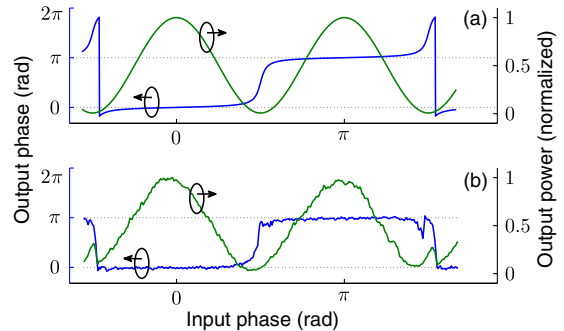

Fig. 2.   (Color online) (a) Analytical and (b) experimental phase-to-amplitude and phase-to-phase transfer functions of a nondegenerate-idler PSA with a maximum of 11 dB of on–off gain.
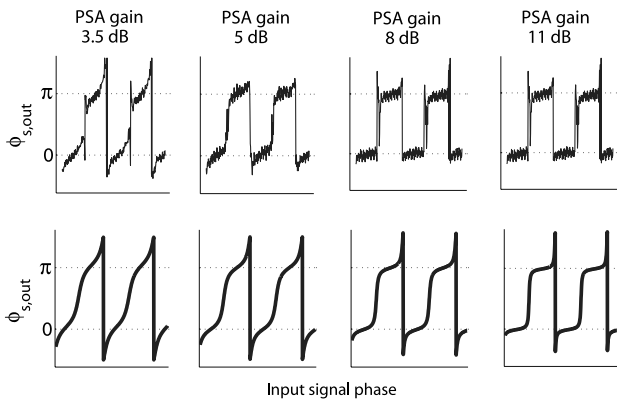
Fig. 3. Experimental (top) and analytical phase-to-phase transfer functions of a nondegenerate PSA for different on–off gains, controlled by changing the pump power.
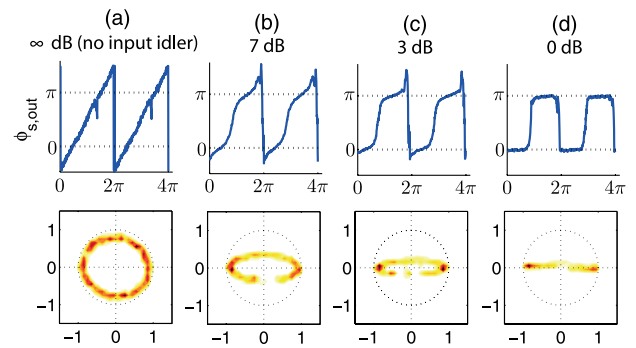

Fig. 4. (Color online) Experimental phase-to-phase transfer functions and output signals in the complex plane of a nondegenerate PSA for different signal-to-idler power ratio at the PSA input.

software to reduce the distortion from the SBS-suppression pump PM. The phase-to-phase transfer is close to being two discrete output states, while the amplitude becomes sinusoidally modulated with input signal phase. It is worth pointing out that a phase change of $\pi/2$ of the signal and idler switches the output amplitude between the maximum and minimum states. Note also that the "overshoots" in the phase-to-phase function are only a result of phase wrapping between 0 and 2π.

In Fig. 3, the phase-to-phase transfer curves calculated from Eq. (3) and measured experimentally (top) are shown for different pump power levels, leading to different values of g_0, and thus different maximum gain and squeezing efficiency. The gain and phase squeezing are closely related and, as the gain tends toward unity, the PSA approaches full phase-preserving behavior, while as the gain becomes larger, the squeezing becomes more efficient around two discrete states, although the PSA clearly shows an efficient phase squeezing property even for moderate gains. Again, the agreement between measured data and theory is very good.

Similar behavior results when instead changing the input signal-to-idler power ratio. Figure 4 shows measured phase-to-phase transfer curves together with measured complex-plane plots of the signal for different power ratios. In Fig. 4(a), there is no idler present at the input, thus giving fully phase-preserving PI operation, and in Figs. 4(b)–4(d), the ratios are 7, 3, and 0 dB, respectively. From the complex-plane plots, the squeezing effect can be seen as the signal being squeezed from the unit circle to the real axis.

We have shown the first, to our knowledge, experimental investigation of the transfer characteristics of nondegenerate-idler PSAs, with excellent agreement with theory. The large amplitude change with phase,

the efficient phase squeezing even for moderate gains, and the factor of 2 higher phase sensitivity compared with conventional interferometers may mean that the phase-to-phase and phase-to-amplitude response of PSAs can be exploited in a variety of interferometric applications, in addition to regeneration of phase encoded data.

References

1. P. A. Andrekson, C. Lundström, and Z. Tong, in *Proceedings European Conference on Optical Communications 2010* (IEEE, 2010), paper We.6.E.1.
2. J. Kakande, C. Lundström, P. A. Andrekson, Z. Tong, M. Karlsson, P. Petropoulos, F. Parmigiani, and D. J. Richardson, Opt. Express **18**, 4130 (2010).
3. K. Croussore and G. Li, IEEE J. Sel. Top. Quantum Electron. **14**, 648 (2008).
4. C. M. Caves, Phys. Rev. D **26**, 1817 (1982).
5. Z. Tong, C. Lundström, P. A. Andrekson, C. J. McKinstrie, M. Karlsson, D. J. Blessing, E. Tipsuwannakul, B. J. Puttnam, H. Toda, and L. Grüner-Nielsen, Nat. Photon. **5**, 430 (2011).
6. R. Slavík, F. Parmigiani, J. Kakande, C. Lundström, M. Sjödin, P. A. Andrekson, R. Weerasuriya, S. Sygletos, A. D. Ellis, L. Grüner-Nielsen, D. Jakobsen, S. Herstrøm, R. Phelan, J. O'Gorman, A. Bogris, D. Syvridis, S. Dasgupta, P. Petropoulos, and D. J. Richardson, Nat. Photon. **4**, 690 (2010).
7. C. McKinstrie and S. Radic, Opt. Express **12**, 4973 (2004).
8. C. Lundström, B. J. Puttnam, Z. Tong, M. Karlsson, and P. A. Andrekson, in *Proceedings European Conference on Optical Communications 2010* (IEEE, 2010), paper Th.10.C.1.